

Characterizing Physical Properties of Superparamagnetic Nanoparticles in Liquid Phase Using Brownian Relaxation

Kai Wu, Karl Schliep, Xiaowei Zhang, Jinming Liu, Bin Ma, and Jian-Ping Wang*

Superparamagnetic iron oxide nanoparticles (SPIONs) have been extensively used as bioimaging contrast agents, heating sources for tumor therapy, and carriers for controlled drug delivery and release to target organs and tissues. These applications require elaborate tuning of the physical and magnetic properties of the SPIONs. The authors present here a search-coil-based method to characterize these properties. The nonlinear magnetic response of SPIONs to alternating current magnetic fields induces harmonic signals that contain information of these nanoparticles. By analyzing the phase lag and harmonic ratios in the SPIONs, the authors can predict the saturation magnetization, the average hydrodynamic size, the dominating relaxation processes of SPIONs, and the distinction between single- and multicore particles. The numerical simulations reveal that the harmonic ratios are inversely proportional to saturation magnetizations and core diameters of SPIONs, and that the phase lag is dependent on the hydrodynamic volumes of SPIONs, which corroborate the experimental results. Herein, the authors stress the feasibility of using search coils as a method to characterize physical and magnetic properties of SPIONs, which may be applied as building blocks in nanoparticle characterization devices.

K. Wu, J. Liu, Prof. J.-P. Wang
The Center for Micromagnetics and Information
Technologies (MINT)
Department of Electrical and Computer Engineering
University of Minnesota
Minneapolis, MN 55455, USA
E-mail: jpwang@umn.edu

Dr. K. Schliep
Department of Chemical Engineering and Material Science
University of Minnesota
Minneapolis, MN 55455, USA


X. Zhang
School of Physics and Astronomy
University of Minnesota
Minneapolis, MN 55455, USA

Prof. B. Ma
Department of Optical Science and Engineering
Fudan University
Shanghai 200433, P. R. China



1. Introduction

Ferrofluids, composed of monodisperse magnetic nanoparticles (MNPs) in aqueous solutions, have been widely used in clinical and medical applications such as drug targeting and delivery, magnetic particle imaging (MPI), and magnetic hyperthermia therapy, etc.^[1–10] These applications exploit the nonlinear magnetic responses of MNPs to alternating current (AC) magnetic fields.^[11–13] Superparamagnetic iron oxide nanoparticles (SPIONs) possessing strong magnetic moments that saturate at relatively low fields on the order of tens of milliteslas are among the most widely used constituents of the ferrofluidic magnetoresponsive nanosystems listed above.^[14,15] Patient safety is one of the most important motivations for choosing SPIONs designed for both therapy and diagnosis.^[16–18] Nowadays, SPIONs can be readily functionalized with polymer shells to ensure colloidal stability and biocompatibility.^[19–21] Due to the large variability in medical treatments and uses, SPIONs have to be specifically tailored for every type of application. For example, MNPs with large magnetic moments are desirable for drug delivery, MRI, and

 The ORCID identification number(s) for the author(s) of this article can be found under <http://dx.doi.org/10.1002/sml.201604135>.

DOI: 10.1002/sml.201604135

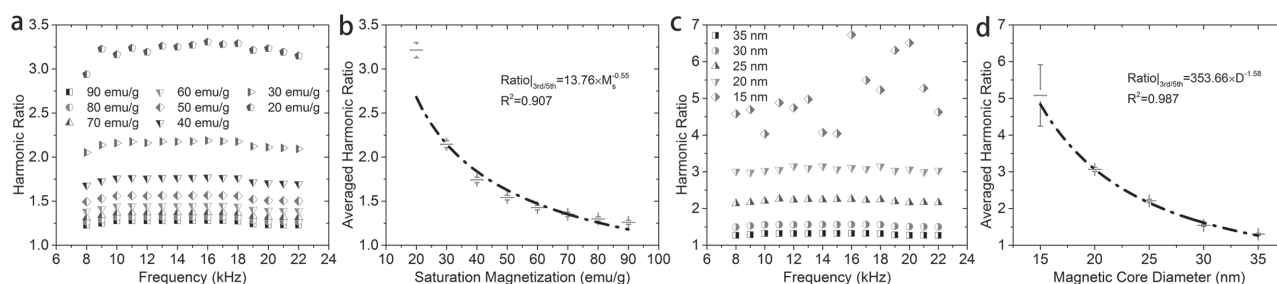


Figure 1. a) Simulated harmonic ratios as a function of frequency with $D = 30$ nm, effective anisotropy constant $K_{\text{eff}} = 1.8 \times 10^5 \text{ erg cm}^{-3}$ ($1.8 \times 10^4 \text{ J m}^{-3}$), and M_s of SPIONs varies from 20 to 90 emu g^{-1} . b) Averaged harmonic ratios as function of M_s . Curve fitting gives rise to $R_{|3\text{rd}/5\text{th}} = 13.76 \times M_s^{-0.55}$, with a coefficient of determination (R^2) of 0.907. c) Simulated harmonic ratios for different SPION core sizes with identical $M_s = 50 \text{ emu g}^{-1}$ as a function of high frequency. d) Averaged harmonic ratios as a function of D . Curve fitting gives rise to $R_{|3\text{rd}/5\text{th}} = 353.66 \times D^{-1.58}$, with a coefficient of determination (R^2) of 0.987.

MPI, so the external gradient field is able to guide MNPs to target tissues.^[22,23] However, MRI needs relatively small particles for in vivo cell tracking, while drug delivery requires larger particles to ensure high magnetic moments.^[22,24–26] Additionally, magnetic hyperthermia treatments preferentially use MNPs that display fast Néel rotation to maximize heating efficiency, yet in biosensing areas Brownian motion is preferred to monitor real-time conjugation of target biomolecules.^[2,10,27–29] Therefore, it is essential to distinguish between SPION sizes, magnetic strength, and even the origin of their superparamagnetism—from intrinsic Néel motion (rotating spin inside a stationary particle) or extrinsic Brownian motion (rotating the entire particle along with its spin).^[11,30,31] Hence, there is a great need for an inexpensive, reliable, fast, and easy-to-use technique to characterize MNPs in aqueous solutions.

Herein, we report a frequency-mixing-method-based search-coil system to characterize both the magnetic and physical properties of SPIONs (the system setup, signal chain, and design of search coils can be found in Notes S1 and S2 in the Supporting Information).^[2,12,13,32] Due to the nonlinear magnetic response of SPIONs, frequency mixing components are induced at odd harmonics exclusively (the dynamic magnetization model can be found in Note S3 in the Supporting Information).^[33] Harmonic ratios of the 3rd over the 5th harmonic are inversely proportional to saturation magnetization, M_s , and magnetic-core diameter, D , of MNPs (the induced-signal model and harmonic-ratio model can be found in Notes S4 and S5 in the Supporting Information). Phase lag of magnetic moment to the driving fields can be monitored by harmonic-phase angles and it contains the information of hydrodynamic volumes of SPIONs (the relaxation-time model and phase-lag model can be found in Notes S6–S8 in the Supporting Information).^[2,34–39]

2. Results and Discussion

Numerical Matlab simulations conforming to our experimental design were performed to reveal the correlation between harmonic ratio and M_s as well as D . A SPION system obeying the log-normal size distribution with average D of 30 nm, standard deviation of 10 nm, surface polymer coating thickness of 4 nm, concentration of 300 pmole mL^{-1} is assumed and tested at room temperature of $T = 300$ K. Two sinusoidal

fields are applied to SPION system: one with amplitude of 100 Oe (7958 A m^{-1}) and frequency of 50 Hz, the other with amplitude of 10 Oe (795.8 A m^{-1}) and its frequency was swept from 8 to 22 kHz. White noise and $1/f$ noise were added in our simulation. Due to crystal asymmetry on the surface of MNPs (spin-canting effect), a smaller M_s and a larger effective anisotropy constant K_{eff} are expected in SPIONs compared to the bulk magnetite.^[40–42] Herein, we vary M_s from 20 emu g^{-1} ($1.05 \times 10^5 \text{ A m}^{-1}$) to 90 emu g^{-1} ($4.72 \times 10^5 \text{ A m}^{-1}$) in our simulation. Data were collected during 0.1 s with a sampling rate of 1 MHz, a discrete Fourier transform was performed on these discrete-time harmonic signals by applying a Hanning window. The harmonic ratios are plotted in Figure 1a as function of frequency for 30 nm SPIONs with different M_s .

Curve fitting to the averaged harmonic ratios versus M_s in Figure 1b shows that the harmonic ratios are inversely proportional to the 0.55th power of M_s . From the simulation results, we can safely conclude that for MNPs with identical core diameters, a smaller harmonic ratio corresponds to a higher M_s . In the second part of our simulation, we set $M_s = 50 \text{ emu g}^{-1}$ as a constant, core size D varies from 15 to 35 nm. The harmonic ratios from different core sizes are summarized in Figure 1c as function of frequency. Curve fitting in Figure 1d shows that harmonic ratio is inversely proportional to the 1.58th power of D . Therefore, for MNPs with identical M_s , a smaller core size yields a larger harmonic ratio. The simulation results give us a simplified formula of harmonic ratio

$$R_{|3\text{rd}/5\text{th}} \sim M_s^{-0.55} \times D^{-1.58} \quad (1)$$

To demonstrate the functionality of our new method, four commercially available SPION samples (purchased from Ocean NanoTech Inc. and Miltenyi Biotec.) were measured using our search-coil system and compared with standard methods. These four samples are: SHP25 (SPIONs with average core size of 25 nm coated with ≈ 4 nm of oleic acid and amphiphilic polymer shells, dispersed in 0.02% sodium azide, 290 pmole mL^{-1}); SMG30-II (SPIONs with average core size of 30 nm, coated with ≈ 6 nm of amphiphilic polymer and PEG shells, dispersed in 0.02% sodium azide, 34 pmole mL^{-1}); SMG30-I are aged SMG30-II; MACS (small SPIONs embedded in matrix, the average overall size is 50 nm, coated with streptavidin, dispersed in 0.05% sodium azide, 3.14 pmole mL^{-1}).^[43] The concentrations of these SPION

samples are below 290 pmol mL^{-1} and the volume concentration is calculated to be less than 0.13 vol%, which is low enough to safely rule out the dipolar interactions and can be treated as a noninteracting system.^[44–48] Amplitudes and phases of the 3rd and the 5th harmonics were measured from four SPION samples. And then the magnetic and physical properties of SPIONs were concluded and compared with standard characterization methods: dynamic light scattering (DLS), transmission electron microscopy (TEM), vibrating sample magnetometer (VSM), X-ray diffractometer (XRD), and high-angle annular dark field-scanning transmission electron microscope-energy dispersive X-ray spectroscopy (HAADF-STEM-EDS).

Magnetic dynamics of single-core MNPs dispersed in a viscous solution are quite different from multicore beads.^[49–53] For single-core MNPs, small SPIONs relax via a Néel process, whereas larger SPIONs relax via a Brownian process. The cut off size between these two processes for single-core SPIONs is around 12 nm. If, instead the SPIONs are embedded in a matrix with overall size of 50 nm, then the cut off size for multicore is around 15 nm (simulated relaxation times as function of core diameters can be found in Note S7 in the Supporting Information). Herein, we are using single-core SPIONs with core diameters larger than 20 nm, thus Brownian process will dominate and phase lag is proportional to hydrodynamic volume. For those multicore beads (SPIONs imbedded in a matrix, such as MACS microbeads), SPIONs will go through the Néel process.^[37] **Figure 2a** shows the measured harmonic ratios of the four SPION samples using our search coil system. From the measured harmonic ratios we anticipate that SMG30-II would have the highest M_s while SMG30-I would have the lowest. SMG30-I, -II, and SHP25 are single-core SPIONs that go through Brownian relaxation; therefore, their phase lag is directly related to their relative hydrodynamic volumes. In **Figure 2b**, we can conclude that SMG30-I and -II have almost the same hydrodynamic volumes and SHP25 comes in second. If we look at the phase lag, we might think that MACS has the smallest hydrodynamic volume; this however, is not the case. Because MACS beads are composed of smaller SPIONs embedded in a matrix, this phase lag is due to the Néel process. By freezing up the aqueous SPION samples, we can effectively block the Brownian rotation, thus all the SPIONs will display Néel relaxation, exclusively. In this way, the multicore magnetic beads would have similar magnetic response both in liquid and frozen states, while the single-core MNPs would have completely different magnetic responses between these two states.

In **Figure 3**, we compared the harmonic ratios and phase lag of MACS and SMG30-II samples both in liquid and frozen states. For MACS beads, SPIONs are immobilized in a matrix and Néel relaxation dominates, regardless of which state it was in (see **Figure 3e**). In contrast, SMG30-II primarily exhibited Brownian relaxation in the liquid state (see **Figure 3f**) and Néel relaxation in the frozen state. Thus, due to the great differences in phase lags and harmonic ratios between liquid and frozen states shown in **Figure 3c,d** we can distinguish between single- and multicore SPIONs.

Based on experimental results in **Figures 2 and 3**, we can estimate the magnetic and physical properties of these samples by using a search-coil system. In summary, SMG30-II would have the highest M_s , followed by SHP25, and SMG30-I

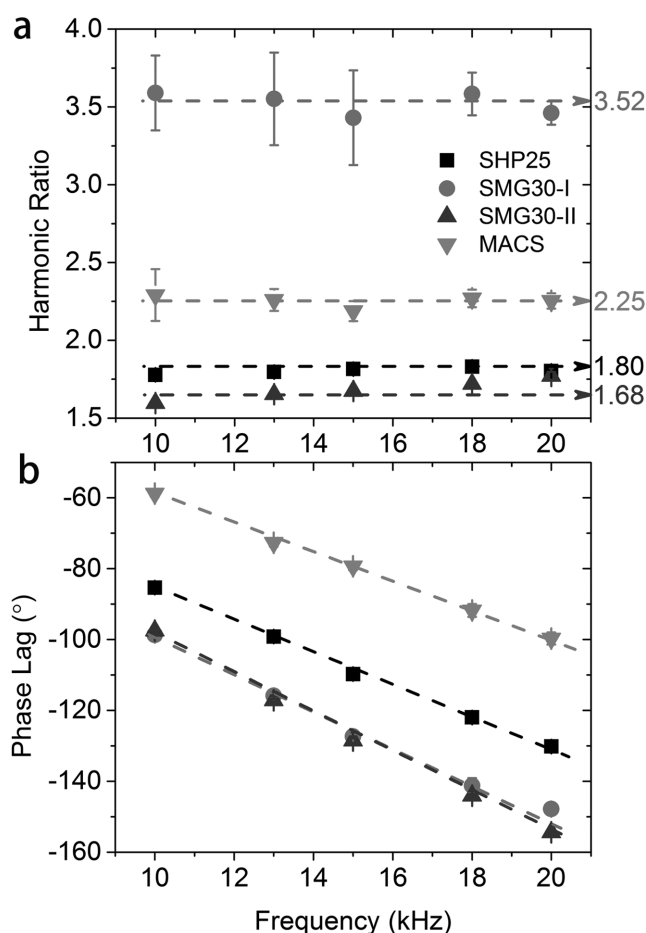


Figure 2. a) Measured harmonic ratios from SHP25, SMG30-I, -II, and MACS samples as function of frequency. b) Measured phase lags at the 3rd harmonics as function of frequency (the phasor theory, sample preparation, experimental method, and data-processing method can be found in Notes S9 and S10 in the Supporting Information).

to have the lowest M_s . Samples SMG30-I and -II are expected to have similar hydrodynamic volumes and are larger than SHP25. The aforementioned SPION samples (SHP25, SMG30-I, and -II) were also determined to be single-cored by measuring their harmonic signals in liquid and frozen states. The MACS sample, however, is expected to be multicored with average magnetic-core diameters of 10 nm (the magnetic-core diameter distribution of MACS, SHP25, SMG30-I, and -II can be found in Note S11 in the Supporting Information). Since the harmonic ratio is inversely proportional to the 0.55th power of M_s , MACS is expected to have lower M_s than SMG30-II and SHP25. So the M_s of these single-core SPION samples from highest to lowest are: SMG30-II > SHP25 > SMG30-I > MACS. The average hydrodynamic sizes followed in descending orders are: SMG30-II \approx SMG30-I > SHP25.

The SPION samples were drop-cast onto supporting carbon grids and air dried to be investigated by TEM. The bright-field TEM micrographs confirmed the spherical morphology in our samples (see **Figure 4a–c**), and further confirmed that SHP25, SMG30-I, and -II are single-core particles. **Figure 4d** shows that each MACS bead is composed of smaller magnetic nanoparticles embedded in a large matrix. The hydrodynamic sizes of these SPION samples in liquid

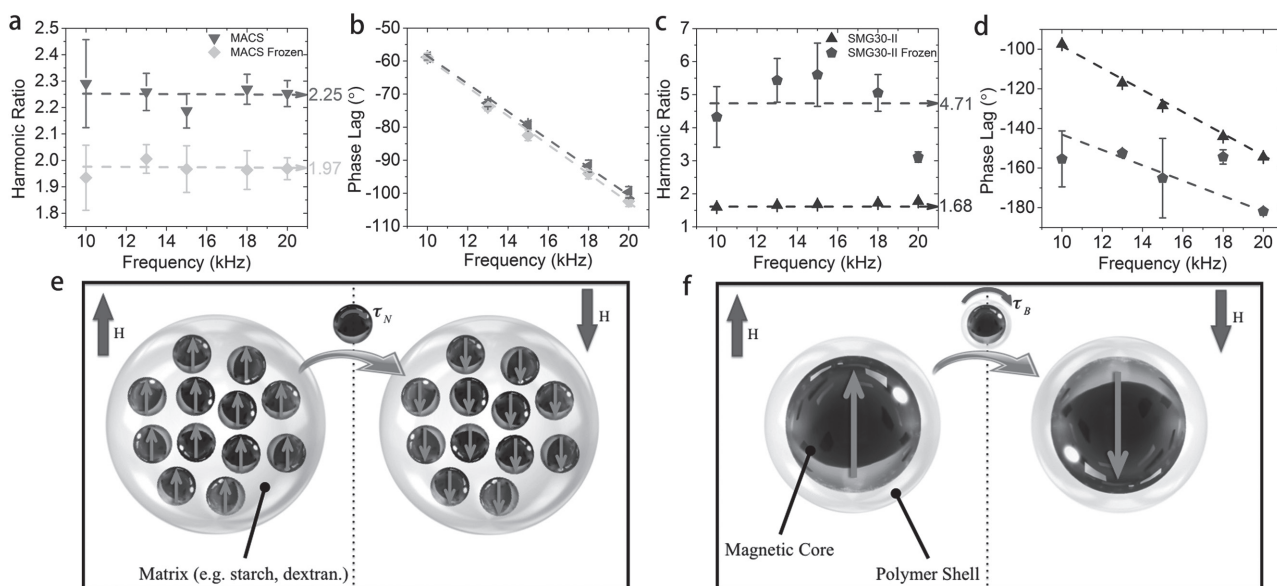


Figure 3. Measured harmonic ratios and phase lag of MACS and SMG30-II SPION samples in liquid and frozen states. a) Comparison of harmonic ratios and b) phase lags between liquid and frozen MACS. c) Comparison of harmonic ratios and d) phase lags between liquid and frozen SMG30-II. e) Néel relaxation process for SPIONs embedded in a matrix under AC fields, both in liquid and frozen states. f) For SMG30-II in liquid state, SPIONs can rotate freely and the Brownian relaxation process dominates under AC fields. By freezing the SPIONs, they are immobilized, thus only the Néel relaxation process is possible. The amplitude of the 3rd harmonic barely changed in frozen MACS, while it dropped by $\approx 98\%$ in frozen SMG30-II compared to liquid state, respectively (summarized data, experimental method, and the analysis can be found in Note S10 in the Supporting Information).

states are tested by DLS. Statistic results from Figure 4e–h give us the mean hydrodynamic sizes of SHP25, SMG30-I, -II, and MACS: 36.90, 40.20, 40.06, and 61.92 nm, respectively. The results from DLS are in good agreement with our search coil based results and analysis. It is worth mentioning that the DLS result of MACS in Figure 4h differs greatly from TEM image in Figure 4d, which is due to the flattening of the matrix during TEM specimen preparation.

The crystalline structure of these SPION samples is characterized by D8 X-ray diffractometer using Cu $K\alpha_1$ radiation ($\lambda = 0.15406$ nm) at a rate of 2° min^{-1} . All diffraction peaks

in Figure 5a are consistent with the standard XRD pattern of magnetite for SHP25, SMG30-I, and -II. The XRD pattern of MACS shows that the particles from these beads are mainly composed of $\alpha\text{-Fe}_2\text{O}_3$ and Fe_3O_4 , which well explained that MACS has the lowest M_s . The TEM diffraction patterns in Figure 5c,d further confirmed our conclusion from XRD data that the nanoparticles from SHP25 are composed of magnetite, and MACS are a mixture of $\alpha\text{-Fe}_2\text{O}_3$ and Fe_3O_4 . In Figure 5b, all of these SPION samples show superparamagnetism, and the saturation magnetization from highest to lowest are: SMG30-II, SHP25, SMG30-I, MACS; which

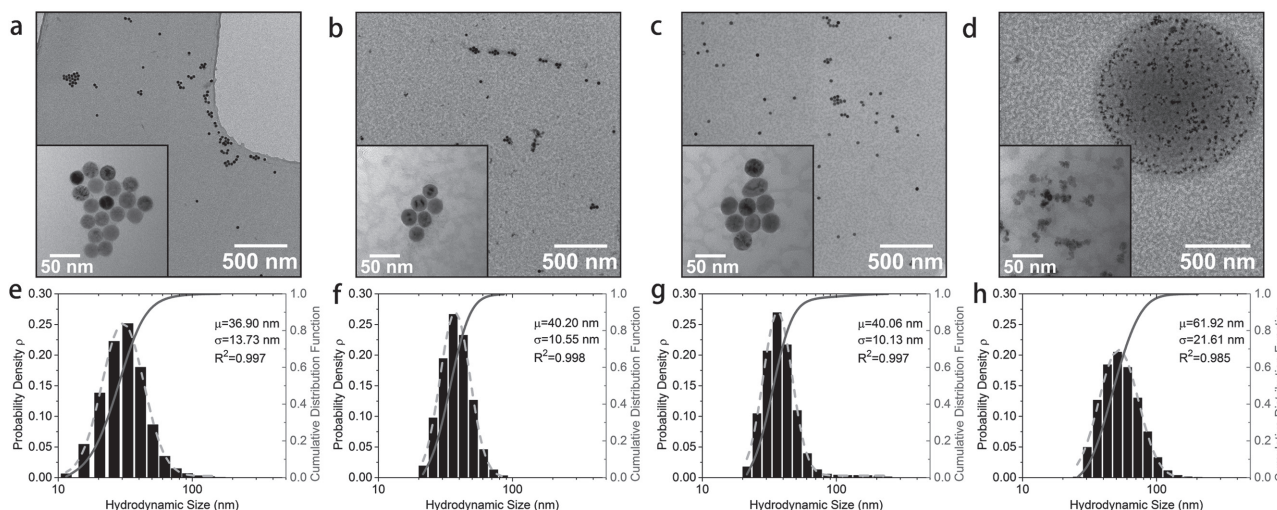


Figure 4. Bright-field TEM micrographs and statistical hydrodynamic size distribution collected using DLS of a,e) SHP25, b,f) SMG30-I, c,g) SMG30-II, and d,h) MACS. Where dashed lines are fitted log-normal size distribution curves, solid lines are cumulative distribution curves, and μ and σ denote the mean and standard deviation of the hydrodynamic sizes (statistics on magnetic-core-diameter distributions can be found in Note S11 in the Supporting Information).

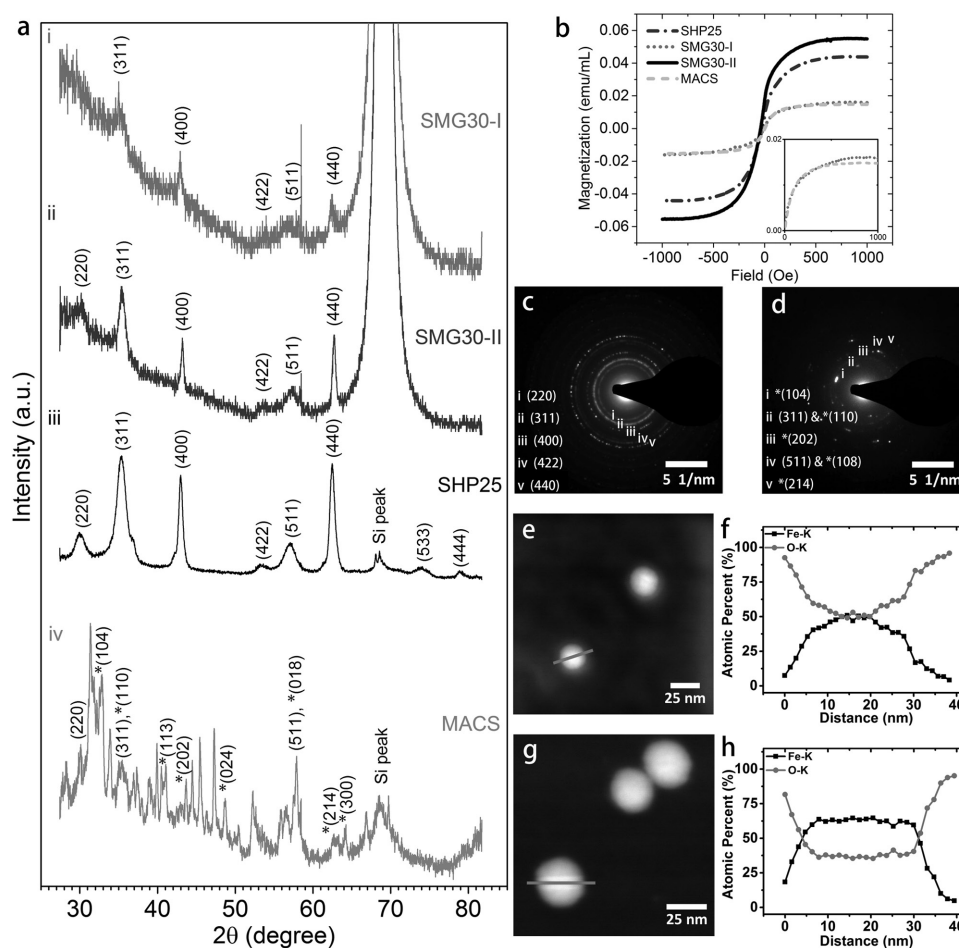


Figure 5. a) XRD spectrum of four air-dried SPION samples, where (i–iv) correspond to diffraction patterns from air-dried SMG30-I, -II, SHP25, and MACS, respectively. Characteristic peaks from Fe_3O_4 are labeled in this figure, and the asterisks denote peaks from $\alpha\text{-Fe}_2\text{O}_3$. b) Magnetization curves of four SPION samples tested at room temperature by VSM. The applied field sweeps from -1000 to 1000 Oe. c, d) TEM diffraction patterns of SHP25 and MACS samples, respectively. e, g) HAADF–STEM–EDS mapping images of SMG30-I and -II, respectively. f, h) Cross-sectional compositional line profiles as marked in (e) and (g), respectively.

agrees well with our search coil based experiments and analysis. The compositional line profiles from Figure 5e–h give us intuitive statistical results of the elemental composition of iron and oxygen in SMG30-I and -II. Due to the aging effect, in SMG30-I the atomic percent of oxygen increases and

meanwhile the iron decreases by the same amount compared to SMG30-II, which explains the lower M_s found in SMG30-I. **Table 1** lists a more detailed comparison between the predicted physical properties from our search-coil system and the measured results from standard characterization methods.

Table 1. Comparison between predicted and measured physical properties.

Physical properties		SHP25	SMG30-I	SMG30-II	MACS
Saturation magnetization	Predicted ^{a)}	+	–	++	--
	Measured by VSM	+	–	++	--
	Measured by XRD	Fe_3O_4	Fe_3O_4	Fe_3O_4	$\alpha\text{-Fe}_2\text{O}_3$ and Fe_3O_4
	Measured by HAADF–STEM–EDS	NA	Fe 50% O 50%	Fe 63% O 37%	NA
Average hydrodynamic size	Predicted	–	+	+	++
	Measured by DLS [nm]	36.90	40.20	40.06	61.92
Dominating relaxation process	Predicted	Brownian	Brownian	Brownian	Néel
	Measured by TEM	Single core	Single core	Single core	Multicore

^{a)} ++, +, –, -- indicate from the highest to the lowest.

3. Conclusions

In summary, herein we proposed a search-coil-based frequency-mixing method to characterize the intrinsic properties of SPIONs such as saturation magnetizations, hydrodynamic sizes, dominating relaxation processes, and physical morphologies (single- or multicore). We have built up a harmonic ratio model (Note S5, Supporting Information), which showed that the saturation magnetization of SPIONs was inversely proportional to the harmonic ratio. Furthermore, the numerical Matlab simulations conforming to our experiment designs were carried out. Theoretically, the harmonic ratio is inversely proportional to the 1.58th power of D and the 0.55th power of M_s . Based on the solid harmonic ratio model and simulation results, we carried out experimental measurements on four commercially available SPION samples. Based on the measured harmonic ratios from our search-coil system we anticipated that SMG30-II would have the highest M_s , followed by SHP25 and SMG30-I, while MACS would have the lowest. The saturation magnetizations from VSM agreed well with our search-coil-based experiments and analysis. The XRD pattern further explained the low M_s found in MACS beads, which was due to the composition of $\alpha\text{-Fe}_2\text{O}_3$ in Fe_3O_4 . HAADF-STEM-EDS mapping images explained the aging effect in SMG30-I, which contributed to a lower M_s compared to SMG30-II. All the measurement results from VSM, XRD, and HAADF-STEM-EDS confirmed and explained the different saturation magnetizations in SPION samples, and agreed well with the predicted relative magnitudes of M_s from harmonic ratios.

Furthermore, since the phase lag is directly related to relative hydrodynamic volumes of SPIONs. We have successfully predicted the relative hydrodynamic sizes of these four SPION samples using the search-coil system, which was later confirmed by DLS results. We demonstrated the feasibility of distinguishing single- and multicore SPIONs by exploring the harmonic ratio and phase lag information from liquid and frozen states. This method is also capable of analyzing which relaxation process dominates for the superparamagnetism. Search coil is a promising method for characterizing physical and magnetic properties of superparamagnetic nanoparticles, which may be applied as building blocks in nanoparticle characterization devices in the future.

Supporting Information

Supporting Information is available from the Wiley Online Library or from the author.

Acknowledgements

The authors thank the support from the Institute of Engineering in Medicine, National Science Foundation MRSEC facility program, the Distinguished McKnight University Professorship, UROP program, MNDrive STEM program, MNDrive program, and the Interdisciplinary

Doctoral Fellowship from the University of Minnesota. Parts of this work were carried out in the Characterization Facility, University of Minnesota, a member of the NSF-funded Materials Research Facilities Network (www.mrfn.org) via the MRSEC program.

Conflict of Interest

The authors declare no conflict of interest.

- [1] N. Lee, T. Hyeon, *Chem. Soc. Rev.* **2012**, *41*, 2575.
- [2] K. Wu, J. Liu, Y. Wang, C. Ye, Y. Feng, J.-P. Wang, *Appl. Phys. Lett.* **2015**, *107*, 053701.
- [3] A. M. Rauwerdink, J. B. Weaver, *Med. Phys.* **2010**, *37*, 2587.
- [4] V. V. Mody, A. Cox, S. Shah, A. Singh, W. Bevins, H. Parihar, *Appl. Nanosci.* **2014**, *4*, 385.
- [5] A. Riedinger, P. Guardia, A. Curcio, M. A. Garcia, R. Cingolani, L. Manna, T. Pellegrino, *Nano Lett.* **2013**, *13*, 2399.
- [6] R. M. Ferguson, A. P. Khandhar, K. M. Krishnan, *J. Appl. Phys.* **2012**, *111*, 07B318.
- [7] K. Murase, *arXiv:1606.03188 [physics.med-ph]* **2016**.
- [8] I. Andreu, E. Natividad, L. Solozábal, O. Roubeau, *ACS Nano* **2015**, *9*, 1408.
- [9] A. Meffre, B. Mehdaoui, V. Kelsen, P. F. Fazzini, J. Carrey, S. Lachaize, M. Respaud, B. Chaudret, *Nano Lett.* **2012**, *12*, 4722.
- [10] S. Laurent, S. Dutz, U. O. Häfeli, M. Mahmoudi, *Adv. Colloid. Interface Sci.* **2011**, *166*, 8.
- [11] S. A. Shah, D. B. Reeves, R. M. Ferguson, J. B. Weaver, K. M. Krishnan, *Phys. Rev. B* **2015**, *92*, 094438.
- [12] H.-J. Krause, N. Wolters, Y. Zhang, A. Offenhäusser, P. Miethe, M. H. Meyer, M. Hartmann, M. Keusgen, *J. Magn. Magn. Mater.* **2007**, *311*, 436.
- [13] P. I. Nikitin, P. M. Vetoshko, T. I. Ksenevich, *J. Magn. Magn. Mater.* **2007**, *311*, 445.
- [14] S. K. Mishra, B. Kumar, S. Khushu, R. P. Tripathi, G. Gangenahalli, *Contrast Media Mol. Imaging* **2016**, *11*, 350.
- [15] H. Graczyk, L. C. Bryan, N. Lewinski, G. Suarez, G. Coullerez, P. Bowen, M. Riediker, *J. Aerosol Med. Pulm. Drug Delivery* **2015**, *28*, 43.
- [16] E. Tombácz, R. Turcu, V. Socoliuc, L. Vékás, *Biochem. Biophys. Res. Commun.* **2015**, *468*, 442.
- [17] H. Arami, A. Khandhar, D. Liggitt, K. M. Krishnan, *Chem. Soc. Rev.* **2015**, *44*, 8576.
- [18] S. J. Soenen, M. De Cuyper, *Nanomedicine* **2010**, *5*, 1261.
- [19] E. Amstad, M. Textor, E. Reimhult, *Nanoscale* **2011**, *3*, 2819.
- [20] M. Szekeres, I. Y. Tóth, E. Illés, A. Hajdú, I. Zupkó, K. Farkas, G. Oszlanczi, L. Tiszlavicz, E. Tombácz, *Int. J. Mol. Sci.* **2013**, *14*, 14550.
- [21] M. Colombo, S. Carregal-Romero, M. F. Casula, L. Gutierrez, M. P. Morales, I. B. Boehm, J. T. Heverhagen, D. Prosperi, W. J. Parak, *Chem. Soc. Rev.* **2012**, *41*, 4306.
- [22] J. Estelrich, E. Escribano, J. Queralt, M. A. Busquets, *Int. J. Mol. Sci.* **2015**, *16*, 8070.
- [23] D. Alcantara, S. Lopez, M. L. García-Martin, D. Pozo, *Nano-medicine* **2016**, *12*, 1253.
- [24] J. Huang, L. Bu, J. Xie, K. Chen, Z. Cheng, X. Li, X. Chen, *ACS Nano* **2010**, *4*, 7151.
- [25] U. I. Tromsdorf, N. C. Bigall, M. G. Kaul, O. T. Bruns, M. S. Nikolic, B. Mollwitz, R. A. Sperling, R. Reimer, H. Hohenberg, W. J. Parak, *Nano Lett.* **2007**, *7*, 2422.
- [26] C. Chouly, D. Pouliquen, I. Lucet, J. Jeune, P. Jallet, *J. Microencapsulation* **1996**, *13*, 245.
- [27] J.-P. Fortin, F. Gazeau, C. Wilhelm, *Eur. Biophys. J.* **2008**, *37*, 223.

- [28] G. F. Goya, E. Lima Jr., A. D. Arelaro, T. Torres, H. R. Rechenberg, L. Rossi, C. Marquina, M. R. Ibarra, *IEEE Trans. Magn.* **2008**, *44*, 4444.
- [29] X. Zhang, D. B. Reeves, I. M. Perreard, W. C. Kett, K. E. Griswold, B. Gimi, J. B. Weaver, *Biosens. Bioelectron.* **2013**, *50*, 441.
- [30] J. Landers, S. Salamon, H. Remmer, F. Ludwig, H. Wende, *Nano Lett.* **2016**, *16*, 1150.
- [31] L. Maldonado-Camargo, I. Torres-Díaz, A. Chiu-Lam, M. Hernández, C. Rinaldi, *J. Magn. Magn. Mater.* **2016**, *412*, 223.
- [32] L. Tu, K. Wu, T. Klein, J.-P. Wang, *J. Phys. D: Appl. Phys.* **2014**, *47*, 155001.
- [33] A. V. Orlov, J. A. Khodakova, M. P. Nikitin, A. O. Shepelyakovskaya, F. A. Brovko, A. G. Laman, E. V. Grishin, P. I. Nikitin, *Anal. Chem.* **2012**, *85*, 1154.
- [34] L. Tu, Y. Jing, Y. Li, J.-P. Wang, *Appl. Phys. Lett.* **2011**, *98*, 213702.
- [35] A. M. Rauwerdink, J. B. Weaver, *Appl. Phys. Lett.* **2010**, *96*, 033702.
- [36] A. M. Rauwerdink, E. W. Hansen, J. B. Weaver, *Phys. Med. Biol.* **2009**, *54*, L51.
- [37] J. Dieckhoff, D. Eberbeck, M. Schilling, F. Ludwig, *J. Appl. Phys.* **2016**, *119*, 043903.
- [38] C. Kuhlmann, A. P. Khandhar, R. M. Ferguson, S. Kemp, T. Wawrzik, M. Schilling, K. M. Krishnan, F. Ludwig, *IEEE Trans. Magn.* **2015**, *51*, 1.
- [39] M. A. Martens, R. J. Deissler, Y. Wu, L. Bauer, Z. Yao, R. Brown, M. Griswold, *Med. Phys.* **2013**, *40*, 022303.
- [40] T. Kim, M. Shima, *J. Appl. Phys.* **2007**, *101*, 09M516.
- [41] G. Goya, T. S. Berquó, F. C. Fonseca, M. Morales, *J. Appl. Phys.* **2003**, *94*, 3520.
- [42] K. Wu, L. Tu, D. Su, J.-P. Wang, *J. Phys. D: Appl. Phys.* **2017**, *50*, 085005.
- [43] W. Wang, Y. Wang, L. Tu, Y. Feng, T. Klein, J.-P. Wang, *Sci. Rep.* **2014**, *4*, 5716.
- [44] F. Ludwig, E. Heim, M. Schilling, *J. Appl. Phys.* **2007**, *101*, 113909.
- [45] C. Djurberg, P. Svedlindh, P. Nordblad, M. F. Hansen, F. Bødker, S. Mørup, *Phys. Rev. Lett.* **1997**, *79*, 5154.
- [46] J. García-Otero, M. Porto, J. Rivas, A. Bunde, *Phys. Rev. Lett.* **2000**, *84*, 167.
- [47] C. Haase, U. Nowak, *Phys. Rev. B* **2012**, *85*, 045435.
- [48] G. T. Landi, *Phys. Rev. B* **2014**, *89*, 014403.
- [49] N. L. Adolphi, D. L. Huber, H. C. Bryant, T. C. Monson, D. L. Fegan, J. Lim, J. E. Trujillo, T. E. Tessier, D. M. Lovato, K. S. Butler, *Phys. Med. Biol.* **2010**, *55*, 5985.
- [50] S. Dutz, J. H. Clement, D. Eberbeck, T. Gelbrich, R. Hergt, R. Müller, J. Wotschadlo, M. Zeisberger, *J. Magn. Magn. Mater.* **2009**, *321*, 1501.
- [51] L. Gutiérrez, R. Costo, C. Grüttner, F. Westphal, N. Gehrke, D. Heinke, A. Fornara, Q. Pankhurst, C. Johansson, S. Veintemillas-Verdaguer, *Dalton Trans.* **2015**, *44*, 2943.
- [52] F. Ludwig, O. Kazakova, L. F. Barquín, A. Fornara, L. Trahms, U. Steinhoff, P. Svedlindh, E. Wetterskog, Q. A. Pankhurst, P. Southern, *IEEE Trans. Magn.* **2014**, *50*, 1.
- [53] N. Usov, B. Y. Liubimov, *J. Appl. Phys.* **2012**, *112*, 023901.

Received: December 14, 2016
 Revised: February 24, 2017
 Published online: April 4, 2017